Research Square

Preprints are preliminary reports that have not undergone peer review.
They should not be considered conclusive, used to inform clinical practice,
or referenced by the media as validated information.

Ultra-Stable Dense Packing in High-Elasticity Oxide Glasses

Hirokazu Masai

hirokazu.masai@aist.go.jp

National Institute of Advanced Industrial Science and Technology

Yohei Onodera

National Institute for Materials Science

Koji Kimoto

National Institute for Materials Science

Takahiro Ohkubo

Chiba University

Shinji Kohara

Japan Synchrotron Radiation Research Institute (JASRI)

Research Article

Keywords:

Posted Date: November 12th, 2026

DOI: https://doi.org/10.21203/rs.3.rs-11549056/v1

License: This work is licensed under a Creative Commons Attribution 4.0 International License.
Read Full License

Additional Declarations: No competing interests reported.

Ultra-Stable Dense Packing in High-Elasticity Oxide Glasses

Hirokazu Masai[1,2*] Yohei Onodera[2], Koji Kimoto[2], Takahiro Ohkubo[3], and Shinji Kohara[4,2]

[1] National Institute of Advanced Industrial Science and Technology, 1–8–31 Midorigaoka, Ikeda, Osaka 563–8577, Japan

[2] Center for Basic Research on Materials, National Institute for Materials Science, 1–2–1 Sengen, Tsukuba, Ibaraki 305–0047, Japan

[3] Graduate School & Faculty of Engineering, Chiba University, 1–33 Yayoi-cho, Chiba 263–8522, Japan

[4] Japan Synchrotron Radiation Research Institute (JASRI), 1–1–1 Koto, Sayo-cho, Sayo-gun, Hyogo 679–5198, Japan

Correspondence and requests for materials should be addressed to H.M. (email: hirokazu.masai@aist.go.jp)

Abstract

High elasticity and optical transparency are generally regarded as mutually incompatible in oxide glasses owing to their inherently sparse network structures, rendering their simultaneous realization under industrially viable processing conditions a fundamental challenge. Here, we demonstrate a class of transparent multi-component Al_2O_3–B_2O_3 glasses prepared by a conventional melt-quenching process that exhibit high Young's moduli of ~150 GPa and subsequent controlled heat treatment further enhances the modulus to ~200 GPa. Structural analyses show that glass structure is significantly dense packed which results in kinetic and structural frustrations. We conclude that such structural confusion can be deliberately exploited not only to stabilize the glassy state but also to embed exceptional elastic modulus. This work provides the first experimental evidence that confusion-driven glass design can be generalized to elasticity-by-design in oxide glasses, establishing a new pathway toward high-value glass materials compatible with advanced industrial applications.

Glass is formed by arresting a supercooled liquid, thereby retaining key liquid-like characteristics that underpin its exceptional formability, atomic-scale surface smoothness, and compositional flexibility. These attributes establish glass as a cornerstone materials class for both fundamental science and advanced technologies. As a result, glass has been indispensable in applications ranging from optical components to structural elements, where precise control over shape, composition, and surface quality is required. Mechanical properties such as hardness, Young's modulus, and fracture toughness critically determine the performance of glass in load-bearing and reinforcement applications[1–4]. To date, the mechanical performance of commercial glasses has been predominantly enhanced using physical or chemical strengthening techniques, most notably ion-exchange processes[5–6]. These approaches rely on the formation of a residual compressive stress layer at the surface, balanced by tensile stress in the interior. While highly effective, stress-based strengthening strategies are intrinsically incompatible with ultrathin glass sheets and high-modulus fibres, where the coexistence of compressive and tensile stress layers becomes geometrically or mechanically prohibitive. Consequently, realizing pristine glasses that intrinsically exhibit high Young's modulus and hardness remains a fundamental challenge in materials science.

From a structural perspective, the Young's modulus of oxide glasses has been empirically linked to the bond dissociation energies of constituent oxides and the atomic packing density[7–8]. However, this relationship is complicated by polyamorphism[9], arising from variations in network connectivity and the presence of structural cavities[10]. Even for oxides with comparable bond strengths, differences in short- and intermediate-range order can lead to markedly different elastic responses. These observations underscore that elasticity in glasses is governed not only by local bond strength but also by network architecture across multiple length scales. Despite the difficulty of quantitatively predicting elastic moduli in such polyamorphic systems, a prevailing design strategy has focused on constructing densely-packed networks enriched with oxides exhibiting high bond dissociation energies[1–4, 7–8, 11–13]. Because conventional network-forming oxides[14] possess relatively modest dissociation energies, intermediate oxides such as Al_2O_3, TiO_2, ZrO_2, and Y_2O_3 have frequently been employed to enhance elastic modulus. In particular, four-coordinated AlO_4 units exhibit among the highest metal–oxygen dissociation energies[7,10], and aluminate-based glasses with high Young's modulus have therefore attracted considerable attention. However, the poor glass-forming ability and high melting point of Al_2O_3 severely limit conventional melt-quenching routes, often necessitating containerless techniques such as laser levitation to

suppress crystallization[15–22]. While such methods enable access to exceptionally stiff oxide glasses, they fundamentally restrict scalability and applicability, highlighting a persistent trade-off between elastic performance and manufacturability.

Recently, we demonstrated that TiO_2-containing aluminoborate glasses in the $CaO–Y_2O_3–(Ti,Zr)O_2–Al_2O_3–B_2O_3$ system exhibit Young's moduli exceeding 130 GPa while maintaining a glass transition temperature around 700 °C[23]. These materials occupy a previously inaccessible region of property space, in which high elastic modulus and moderate processing temperatures are simultaneously achieved. Notably, optically transparent bulk glasses with dimensions exceeding several millimetres in thickness and centimetres in diameter were successfully fabricated by a conventional melt-quenching process. The absence of SiO_2 and the high atomic packing densities indicate the formation of unusually dense oxide networks, accompanied by relatively high Poisson's ratios compared with conventional oxide glasses. Although the enhanced Young's modulus has been qualitatively attributed to the high bond dissociation energies of constituting oxides, the structural origins of the high Young's modulus have not yet been clarified.

Here, we propose a reinterpretation of the cation–oxygen contrast in oxide glasses, not simply as a measure of bond strength, but as an elastic mismatch between rigid cation-centric polyhedra and a deformable oxygen subnetwork. From the perspective of Greer's "confusion by design"[24], this pronounced contrast represents a structural origin of kinetic and structural frustration in multicomponent networks[25–28]. In densely packed systems, such confusion suppresses low-energy deformation modes while preserving structural disorder, giving rise to unusually high elastic moduli in the absence of crystallinity. In this view, polyamorphism does not limit elastic performance, but instead provides a heterogeneous structural landscape in which rigid units and flexible substructures coexist and cooperatively define macroscopic elasticity. Extending this concept, we further reinterpret crystallization[29] not as an extrinsic strengthening route, but as a means to lock in and amplify the intrinsic cation–oxygen elastic contrast inherent to the confused glassy network. Controlled crystallization selectively immobilizes rigid cation-centric polyhedra while retaining a continuous oxygen subnetwork, thereby further suppressing low-energy deformation modes and driving a step change in elastic modulus. Crucially, this contrast-fixation pathway enables substantial enhancement of Young's modulus without reliance on surface compression layers, offering a viable route toward transparent, highly stiff glass and glass-ceramic materials compatible with industrial processing.

Results

Monolithic bulk glasses were successfully prepared by conventional melt quenching, building on our previous compositions with Young's moduli of up to 137 GPa[23]. To further enhance elastic stiffness, CaO was substituted by MgO, guided by the dependence of elastic modulus on metal–oxygen bond strength. Systematic compositional comparisons reveal that CaO–MgO substitution increases density, glass transition temperature and Young's modulus without significantly affecting the thermal expansion coefficient (Table 1). Data for glasses with similar compositions are summarized in Supplementary Table 1. The thermal expansion behaviour indicates that high-field-strength oxides such as Y_2O_3, TiO_2, and ZrO_2 dominate volumetric expansion in this system. Despite the higher dissociation energy of ZrO_2 relative to TiO_2, glasses with varying ZrO_2/TiO_2 ratios exhibit comparable elastic moduli, highlighting the critical role of network connectivity beyond bond strength alone. Consistently, ultrasonic and indentation measurements show concomitant increases in sound velocities, elastic moduli and hardness with MgO substitution, yielding a clear linear correlation between Young's modulus and Vickers hardness. These results demonstrate that high stiffness and hardness can be achieved intrinsically through compositional design, without relying on silicate networks or surface-based strengthening.

Thermal stability, optical properties and structural homogeneity of the $MgO{-}Y_2O_3{-}(Ti, Zr)O_2{-}Al_2O_3{-}B_2O_3$ glasses were evaluated to assess their processability and structure–property relationships (Fig. 1). Differential thermal analysis (DTA) reveals pronounced crystallization behaviour, from which the thermal stability parameter $\Delta T = T_x - T_g$ was determined. ID1 and ID2 exhibit large ΔT values exceeding 100 °C, indicating sufficient resistance of the supercooled liquid against crystallization for fibre drawing[30] and melt-based processing, whereas Y_2O_3-rich compositions show reduced thermal stability despite their higher elastic moduli (Table 1). Optical measurements indicate that TiO_2-containing glasses exhibit reduced transparency due to defect-related visible absorption, while partial substitution of TiO_2 by ZrO_2 markedly improves transparency and shifts the absorption edge to higher energy (Fig. 1c). Variations in refractive index (Supplementary Fig. 1) further suggest that optical properties are governed not only by composition but also by network connectivity. Scanning transmission electron microscopy (STEM) and electron diffraction confirm the fully amorphous nature of the glasses, with no evidence of crystallization or phase separation, while subtle intensity modulations in the diffuse halo indicate atomistic density fluctuations embedded within these densely packed oxide networks (Fig. 1d–f). These results demonstrate that these glasses combine high elastic moduli with sufficient thermal

stability and optical homogeneity, despite subtle atomistic density fluctuations within the amorphous network.

Motivated by the anomalous atomistic contrast suggested by STEM observations, diffraction experiments were carried out to probe the structural origin of these features. Fig. 2a presents the X-ray and neutron total structure factors, $S^{X}(Q)$ and $S^{N}(Q)$, of the ID1 glass. While no macroscopic phase separation is detected by STEM, the $S^{X}(Q)$ reveals a pronounced small-angle scattering, indicating the presence of subtle structural fluctuation. The absence of a corresponding feature in the $S^{N}(Q)$ suggests that heavier cations such as Y, Ti, and Zr predominantly contribute to this fluctuation. In the $S^{N}(Q)$, a first sharp diffraction peak (FSDP) appears at $Q = 2.05$ Å^{-1}, associated with the formation of intermediate-range order, commonly observed in AX_2 and A_2X_3 oxide glasses[31,32]. The second principal peak (PP)[32] observed at $Q = 2.90$ Å^{-1} is a benchmark of packing fraction of oxygen atoms. On the other hand, the first peak observed at $Q = 2.30$ Å^{-1} in the $S^{X}(Q)$ is not an FSDP nor PP, suggesting that this peak is a benchmark of packing fraction of heavy cations such as Y, Ti, and Zr. This peak can be often observed in network free oxide glasses prepared by aerodynamics levitation technique[33,34]. It is worth mentioning that the $S^{X}(Q)$ exhibit a significant negative peak at the position of the PP in the $S^{N}(Q)$, which is identical to the dark halo ring observed in STEM. Corresponding reciprocal signatures are also evident in the reduced pair distribution functions, $G^{X,N}(r)$ (Fig. 2b), where peaks in neutron data are observed as a negative peak in the X-ray data. Such behaviours have previously been reported in densely packed oxide glasses and liquids lacking conventional network formers, where extensive edge- and face-sharing polyhedral connectivity gives rise to pronounced chemical contrast[33,34, 35], while such a behaviour was not observed in conventional silicate glasses and liquids[36]. Total correlation functions $T^{X,N}(r)$ (Fig. 2c) further resolve distinct local correlations up to approximately 2 Å, with well-defined B–O and Al–O peaks at 1.38 and 1.79 Å in the neutron data. Furthermore, the third and fourth peaks in $T^{N}(r)$ at 2.39 and 2.87 Å can be attributed to the O–O distances within BO_n[37] and AlO_x[38, 39] motifs, suggesting the formation of BO_n (n = 3 or 4) and AlO_x (x = 4 – 6) polyhedra. Similar results are also observed for the ID2 glass (Supplementary Fig. 2). This behaviour demonstrates that the mixture of BO_n and AlO_x polyhedra generated by conventional network forming oxides plays an important role in the glass, which mirrors the confusion principle[24] in metallic glasses, suggesting a common origin in geometric frustration[27]. Together, the combined diffraction results provide direct evidence for a pronounced contrast between heavy-cation polyhedral units and the surrounding oxygen network, supporting the existence of chemically and elastically heterogeneous motifs embedded within an otherwise

amorphous structure. These reciprocal-space signatures directly reflect the elastic and chemical contrast postulated for densely-packed oxide networks, providing a structural basis for the unusually high Young's modulus discussed below.

To complement the diffraction analysis and probe element-specific local structures, X-ray absorption fine structure (XAFS) and solid-state NMR measurements were performed. The K-edge XANES spectra of Zr, Y and Ti indicate stable tetravalent and trivalent states of these cations in the ID1 glass, consistent with their corresponding oxide references (Fig. 2d–f and Supplementary Fig. 3). Analysis of the EXAFS data reveals that the local coordination environments of Zr and Y closely resemble those in crystalline ZrO_2 and Y_2O_3, whereas Ti exhibits a shorter average Ti–O distance, indicative of a more distorted coordination geometry. This behaviour suggests a higher structural flexibility of Ti–O polyhedra in the glass network[40], reflecting differences in the glass-forming tendencies of the constituent oxides. Figs 2g, h present the ^{11}B and ^{27}Al MAS NMR spectra of the ID1 glass. The ^{11}B spectrum indicates the coexistence of trigonal and tetrahedral boron units[41–43], whereas the ^{27}Al spectrum reveals mixed four-, five-, and six-coordinated aluminium species[42–43]. The relative abundance of each structural unit was quantified from the element-specific data. Fig. 2i shows the abundance of each unit. Notably, the structural units conventionally regarded as glass-network formers account for 54% of the total cations. The coexistence of rigid cation-centric polyhedra and structurally flexible network units provides direct chemical-scale evidence for the pronounced structural contrast inferred from diffraction. These coordination statistics underpin the unusually high elastic modulus and packing density discussed in the following sections. These element-specific structural motifs establish a direct link between chemical-scale heterogeneity and the macroscopic elastic modulus of the glass. Unlike conventional compositional heterogeneity, which relies on spatial segregation, the present system represents a homogeneous yet internally contrasted glass network, in which elastic properties emerge from intrinsic cation–oxygen contrast rather than phase separation.

From a materials design perspective, increasing Young's modulus requires maximizing the fraction of oxides with high metal–oxygen bond dissociation energies, such as Y_2O_3, TiO_2, ZrO_2, and Al_2O_3, while simultaneously suppressing mechanically weak network units such as trigonal boron. However, this approach inevitably compromises glass-forming ability. To overcome this trade-off, we adopted a combined SiO_2–Li_2O substitution strategy. Unlike simple SiO_2 enrichment, which tends to reduce packing density[44], Li_2O–SiO_2 incorporation enhances elastic stiffness while lowering the T_g and preserving melt processability[45]. Consistent with this design

rationale, the present glasses exhibit significantly enhanced elastic properties while remaining vitrifiable by conventional melt quenching, albeit with a moderate reduction in thermal stability (ID3–ID5). Their high atomic packing density (Supplementary Table 2) further supports the view that dense atomic packing is a key structural origin of high elasticity. This insight motivated us to investigate controlled crystallization as an additional route to achieve high modulus while mitigating the trade-off with thermal stability.

Controlled crystallization, defined as the thermal precipitation of crystalline phases within an amorphous matrix, offers a powerful route to decouple mechanical performance from glass-forming constraints[29]. Glass-ceramics produced by appropriate heat treatment can integrate the rigidity of crystalline phases with the processability and structural continuity of a residual glassy matrix. We previously demonstrated that controlled precipitation of TiO_2 crystallites substantially enhances the Young's modulus of aluminoborate glasses, establishing crystallization as an effective strategy for stiffening oxide glasses[46]. X-ray diffraction patterns (Fig. 3a) reveal the emergence of sharp Bragg peaks upon crystallization, with several peak positions coinciding with features already present in the structure factor $S(Q)$ of the pristine glass. In particular, a crystalline reflection at ~1.19 $Å^{-1}$ overlaps with a shoulder in the glass $S(Q)$, indicating that the parent glass contains structural motifs that act as precursors for crystallization. Prominent diffraction peaks assignable to ZrO_2 and $Y_{17.3}B_6O_{34}$ phases further demonstrate that the amorphous network inherently accommodates local environments resembling these crystalline oxides, in agreement with the XANES results. Notably, ZrO_2 is well-known nucleating agents in glass-ceramic systems[47], suggesting that the remaining glass components kinetically suppress crystallization during melt quenching while retaining latent structural order. Inset shows photographs of ID1 glass-ceramics obtained by heat-treatment at different temperatures. Heat-treatment at 800 °C induces a pronounced change from transparent vinous glass to translucent blue glass ceramic while preserving light transmission, indicating nanoscale structural heterogeneity rather than macroscopic opacity. This coloration arose from light scattering associated with nanostructured crystallites embedded in the amorphous matrix. Despite the complexity of diffraction patterns arising from multicomponent crystallization (Fig. 3b), the preferential emergence of crystalline phases represents a distinctive feature of this system. The XRD patterns obtained from the bulk sample and from the powder produced by pulverizing the sample were indistinguishable (Supplementary Fig. 4). This result demonstrates that crystallization progressed homogeneously throughout the interior of the glass, confirming bulk crystallization mechanism rather than surface crystallization. The STEM

images (Supplementary Fig. 5) suggest that glass-ceramic was composed of polycrystalline grains with an average size of approximately 50 nm. ADF observations suggested that the precipitated crystals exhibited compositional heterogeneity, with the constituent elements showing spatial segregation rather than a uniform distribution. Fig. 3c shows 4D-STEM image of $4.5MgO–20Y_2O_3–5TiO_2–10.5ZrO_2–34Al_2O_3–24B_2O_3–1Li_2O–1SiO_2$ (ID4) glass-ceramic heat-treated at 850 °C for 3 h. The electron diffraction patterns obtained from the individual particles, each approximately 10~20 nm in size, indicate that the particles are predominantly single crystalline. The STEM-Electron Energy Loss Spectroscopy (EELS) mappings reveal that atomic-scale compositional heterogeneity was evident (Supplementary Fig. 6). Although oxygen exhibited a nearly uniform spatial distribution, the particles showing brighter contrast in the Annlar dark field (ADF) image were B, Y, and Zr-rich, whereas those exhibiting darker contrast were Mg, Al, and Ti-rich. The observed contrast suggests the existence of two distinct particle populations with elements. This structural motif can be well understood by the schematic illustration shown in Fig. 3d. The orange and purple dotted ellipses schematically indicate precursor regions for crystallization. It is assumed that pristine glass is homogenous at the macroscopic view while a slight atomistic heterogeneity exists as shown in dotted ellipses. The high elastic modulus may originate from crystal-like atomic heterogeneities with a densely packed structure.

As summarized in Fig. 4a, heat-treatment leads to a dramatic increase in Young's modulus to approximately 200 GPa, accompanied by Vickers hardness values exceeding 1200, particularly in Y_2O_3-rich compositions. Achieving an elastic modulus comparable to that of structural metals such as steel while maintaining glass-based processing is a notable outcome. Collectively, these findings establish crystallization as a powerful contrast-engineering strategy that bridges glassy disorder and crystalline rigidity. Crystallization also induces a pronounced decrease (~5%) in Poisson's ratio as shown in Fig. 4b. Because Poisson's ratio reflects not only deformation behaviour but also the availability of structural free volume, this decrease indicates crystallization-induced densification–rarefaction at the nanoscale. These results support a picture in which controlled crystallization selectively immobilizes rigid cation-centric polyhedra, amplifying the intrinsic cation–oxygen elastic contrast of the parent glass and enabling a step change in mechanical performance without relying on surface-based strengthening. Fig. 4c summarizes the Young's modulus of the glasses developed in this study as a function of the glass transition temperature, together with representative data reported previously. Both pristine glasses and glass ceramics obtained by subsequent heat treatment are plotted using the same T_g values.

The present glasses achieve the highest Young's modulus reported to date for melt-derived, large-area oxide glasses. Notably, the glass ceramics exhibit even higher values, reaching elastic moduli on the order of 200 GPa—comparable to that of steel. The inset photograph of the ID4 glass ceramic heat-treated at 850 °C for 3 h demonstrates that a translucent specimen with a thickness of 0.58 mm retains measurable optical transparency, as evidenced by the faint visibility of background text under illumination. This combination of ultra-high Young's modulus and retained light transmission is rarely achieved in oxide glass-based materials. The key advantage of the present materials lies in their unprecedented coupling of a relatively low glass transition temperature with an exceptionally high Young's modulus. By simultaneously optimizing thermal processability and elastic modulus, these glasses access a previously uncharted region of the T_g–Young's modulus property space[1], filling a long-standing gap in the known landscape of oxide glasses. This synergy substantially expands the design freedom of glass materials and enables new classes of glass-based devices that demand both mechanical rigidity and formability.

In summary, we demonstrate that large, transparent oxide glasses with Young's moduli approaching 150 GPa can be fabricated by a conventional melt-quenching process without laser-based processing. Furthermore, controlled crystallization enables a further increase in Young's modulus to approximately 200 GPa while preserving scalability and partial optical transparency. In the concept of Greer's "confusion principle", the present multicomponent oxide networks intentionally frustrate crystallization while preserving dense, rigid local motifs. This confusion not only stabilizes the glassy state but also enables elastic stiffness approaching that of crystalline solids. More broadly, this work reframes "confusion principle" as a general materials design strategy, demonstrating that kinetic frustration can be exploited not only to form glasses but also to engineer extreme elastic properties. This establishes elasticity-by-design as a natural extension of confusion-based glass science. Future advances in structural control are expected to further enable the design of optimised, high-performance oxide glasses composed of ubiquitous elements and synthesized at reduced melting temperatures, reinforcing the role of glass as a high-value structural and functional material. As highlighted by Ritchie[50], strength and toughness are often controlled by distinct mechanisms operating at different length scales. Future studies combining atomic-scale structural characterization with mesoscale analyses of crystallization-induced heterogeneity will be essential for elucidating the origins of the exceptional mechanical performance observed in the present glass–ceramic.

Materials and Methods

The glasses were fabricated using a conventional melt-quenching method in a Pt crucible. The main compositions of the initial materials were MgO (99.9%), Y_2O_3 (99.99%), TiO_2 (99.99%), Al_2O_3 (99.99%), and B_2O_3 (99.99%) (Kojundo Chemical Laboratory, Japan), and the materials were mixed. The following reagents were used to replace TiO_2: MgO (99.9%), La_2O_3 (99.9%), SiO_2 (99.999%), Nb_2O_5 (99.9%), WO_3 (99.9%), ZrO_2 (99.99%), and Ta_2O_5 (99.9%). ZrO_2 was procured from Furuuchi Chemical Corporation (Japan), and all other chemical reagents were obtained from Kojundo Chemical Laboratory (Japan). Prior to mixing, Al_2O_3 and SiO_2 powders were heated separately at 600 °C under reduced pressure for 3 h to remove adsorbed water. The mixture was placed in a Pt crucible, which was then placed in an electric furnace at 1100 °C. The furnace was then heated to 1400–1640 °C at a rate of 500 °C·h^{-1} and maintained at the target temperature for 20 min. After melting for 20 min, the glass melt was quenched on a steel plate heated to 200 °C. The glass sample was then annealed for 1 h in air at the glass-transition temperature (T_g), which was determined using differential thermal analysis (DTA). After annealing, the glass samples were mechanically polished to obtain mirror-like surfaces. The dimensions of each sample were 10 mm × 10 mm × 1 mm.

The scanning transmission electron microscopy (STEM) experiments were conducted using a Thermo Fisher Scientific Titan microscope equipped with two aberration correctors and a monochromator. The microscope was operated at 300 kV under the following standard STEM imaging conditions: The convergence semiangle was 20 mrad, the bright-field detector was 0-5 mrad, and the high-angle annular dark-field detector ranged from 50 to 200 mrad. An electron diffraction pattern was obtained using a Gatan energy filter (Continuum HR) to eliminate background due to inelastic scattering.

As previously reported, T_g and the deformation temperature (T_D) were determined using thermomechanical analysis (TMA; DIL 402, NETZSCH, Germany) with a load of 500 mN and heating rate of 5 °C·min^{-1}. The dimensions of the representative samples used for the TMA were 5 mm ×15 mm × 2–3 mm. The coefficient of thermal expansion (CTE) was calculated in the temperature range of 290–490 °C. DTA measurements were performed using a Thermo plus EVO2 thermal analyser (Rigaku, Japan) to determine T_g, the crystallization-onset temperature (T_x), and the thermal-stability parameter ($\Delta T = T_x - T_g$)[30]. Both bulk and powdered samples were analyzed to evaluate their crystallization behaviour. The ultrasonic velocities of the longitudinal (V_L) and

transverse (V_T) waves were measured at 24 ± 1 °C using the ultrasonic pulse-echo method (DPR300, JSR Ultrasonics, Imaginant, USA). The frequencies of the longitudinal and transverse transducers were 10 and 5 MHz, respectively. The Young's modulus (E_0), instantaneous shear modulus (G_0), bulk modulus (K_0), and Poisson's ratio (v) were calculated based on previously reported methods[1, 51]. The errors associated with E_0, G_0, and K_0 were less than ±0.1 GPa. The density ρ of the glasses was determined using He gas pycnometry (AccuPycII 1340, Micromeritics, USA). Vickers hardness (HV) measurements were performed using a microhardness tester (HM-220, Mitutoyo, Japan) under an air atmosphere at room temperature. All samples underwent 10 indents under a load of 0.2 N with a dwell time of 15 s.

The refractive indices were measured using a prism coupler (Metricon, USA) at 456, 633, 832, and 1545 nm. Absorption spectra of the glasses were measured using a spectrometer (UH4150, Hitachi, Japan). An RINT 2100 X-ray diffractometer (Rigaku, Japan) with Cu K radiation was used to examine the precipitated crystallites in the glass.

The high-energy X-ray diffraction experiment was performed at the BL04B2 beamline at the SPring-8 synchrotron radiation facility, using the diffractometer dedicated to the study of disordered materials[52]. The energy of the incident X-rays was 112.76 keV. The raw data were corrected for polarization, absorption, and background, and the contribution of Compton scattering was subtracted using standard data analysis software[52].

Neutron diffraction measurements were performed on a high-intensity total diffractometer, NOVA[53], installed at BL21 of the Materials and Life Science Experimental Facility at the J-PARC spallation neutron source. Glass samples were put into 6 mm diameter vanadium-nickel null alloy cells. The scattering intensities were corrected for the background absorption and multiple scattering, and normalized with the scattering intensity from a vanadium rod.

Ti K-edge (4.966 keV), Y K-edge (17.038 keV), and Zr K-edge (17.998 keV) XAFS spectra at the BL14B2 beamline of the SPring-8 synchrotron radiation facility (Hyogo, Japan). The XAFS measurements of Ti, Zr, and Y were performed in the transmission mode (Quick Scan method) at 25 °C using a Si (111) and a Si(311) double-crystal monochromator, respectively. Pellet samples for the measurements were prepared by mixing the granular sample with boron nitride. The corresponding analyses were performed using Athena software[54].

The ^{11}B and ^{27}Al magic-angle-spinning (MAS) NMR spectra were acquired using a doubletuned NMR probe and a JEOL Delta spectrometer operating at a magnetic field strength of 18.79 T. The powdered glass samples were packed into 3.2-mm ZrO_2 rotors. The samples were spun at 20 kHz, and the pulse length was set to 0.1 μs, corresponding to a π/12 flip angle. A recycle delay of 5 s was used for both ^{27}Al and ^{11}B to ensure quantitative spectral intensities. The ^{11}B and ^{27}Al MAS NMR spectra were acquired with 128 and 512 scans, respectively. The ^{11}B and ^{27}Al chemical shifts were referenced to 1.0 M H_3BO_3 and 0.1 M $AlCl_3$ aqueous solutions, respectively, at 0.0 and -0.1 ppm. The three- and four-coordinated B sites observed in the ^{11}B MAS NMR spectrum were well separated, and their relative abundances were determined from the integrated peak areas. The experimental ^{27}Al MAS NMR spectrum was simulated using a Czjzek probability density function[55] for the distributions of the isotropic chemical shift and quadrupolar coupling constant. Spectral simulations of the ^{27}Al MAS NMR spectra were performed using an in-house program incorporating mrsimulator[56].

References

1. Rouxel, T. Elastic properties and short- to medium-range order in glasses. *J. Am. Ceram. Soc.* **90**, 3019–3039 (2007).
2. Greaves, G. N., Greer, A. L., Lakes, R. S. & Rouxel T. Poisson's ratio and modern materials. *Nat. Mater.* **10**, 823–837 (2011).
3. Rouxel, T. & Yoshida, S. The fracture toughness of inorganic glasses. *J. Am. Ceram. Soc.* **100**, 4374–4396 (2017).
4. Rodrigues, B. P., To, T., Smedskjaer, M. M. & Wondraczek, L. Mechanical properties of oxide glasses. *Rev. Mineral. Geochem.* **87**, 229–281 (2022).
5. Nordberg, M. E., Mochel, E. L., Garfinkel, H. M. & Olcott, J. S. Strengthening by ion exchange. *J. Am. Ceram. Soc.* **47**, 215–219 (1964).
6. Karlsson, S., Jonson, B. & Stålhandske, C. The technology of chemical glass strengthening: a review. *Glass Technol. Part A* **51**, 41–54 (2010).
7. Makishima, A. & Mackenzie, J. D. Direct calculation of Young's modulus of glass. *J. Non-Cryst. Solids* **12**, 35–45 (1973).
8. Makishima, A. & Mackenzie, J. D. Calculation of bulk modulus, shear modulus and Poisson's ratio of glass. *J. Non-Cryst. Solids* **17**, 147–157 (1975).
9. Angell, C. A., Poole, P. H. & Shao, J. Glass-forming liquids, anomalous liquids, and polyamorphism in liquids and biopolymers. *Nuovo Cimento D* **16**, 993–1025 (1994).
10. Pabst, W. & Gregorová, E. Elastic properties of silica polymorphs – a review. *Ceram. Silikáty* **57**, 167–184 (2013).
11. Inaba, S., Todaka, S., Ohta, Y. & Morinaga, K. Equation for estimating Young's modulus, shear modulus and Vickers hardness of aluminosilicate glasses. *J. Jpn. Inst. Met.* **64**, 177–183 (2000).
12. Inaba, S., Fujino, S. & Morinaga, K. Young's modulus and compositional parameters of oxide glasses. *J. Am. Ceram. Soc.* **82**, 3501–3507 (1999).
13. Sugimura, S., Inaba, S., Abe, H. & Morinaga, K. Compositional dependence of elastic properties of oxide glasses. *J. Ceram. Soc. Jpn.* **110**, 1103–1106 (2002).
14. Sun, K. H. Fundamental condition of glass formation. *J. Am. Ceram. Soc.* **30**, 277–281 (1947).

15. Weber, R., Hampton, D. S., Merkley, D. R., Rey, C. A., Zatarski, M. M. & Nordine, P. C. Aero-acoustic levitation: a method for containerless liquid-phase processing at high temperatures. *Rev. Sci. Instrum.* **65**, 456–465 (1994).

16. Weber, J. K. R., Abadie, J. G., Hixson, A. D., Nordine, P. C. & Jerman, G. A. Glass formation and polyamorphism in rare-earth oxide–aluminum oxide compositions. *J. Am. Ceram. Soc.* **83**, 1868–1872 (2000).

17. Tangeman, J. A., Phillips, B. L., Nordine, P. C. & Weber, J. K. R. Thermodynamics and structure of single- and two-phase yttria–alumina glasses. *J. Phys. Chem. B* **108**, 10663–10671 (2004).

18. Rosales-Sosa, G. A. *et al.* High elastic moduli of a $54Al_2O_3$–$46Ta_2O_5$ glass fabricated via containerless processing. *Sci. Rep.* **5**, 15233 (2015).

19. Rosales-Sosa, G. A., Masuno, A., Higo, Y. & Inoue, H. Crack-resistant Al_2O_3–SiO_2 glasses. *Sci. Rep.* **6**, 23620 (2016).

20. Rosales-Sosa, G. A., Masuno, A., Higo, Y., Watanabe, Y. & Inoue, H. Effect of rare-earth ion size on elasticity and crack initiation in rare-earth aluminate glasses. *J. Am. Ceram. Soc.* **101**, 5030–5036 (2018).

21. Ma, X., Peng, Z. & Li, J. Effect of Ta_2O_5 substitution on thermal and optical properties of high-refractive-index La_2O_3–Nb_2O_5 glasses prepared by aerodynamic levitation. *J. Am. Ceram. Soc.* **98**, 770–773 (2015).

22. Guo, Y. *et al.* High-entropy R_2O_3–Y_2O_3–TiO_2–ZrO_2–Al_2O_3 glasses with ultrahigh hardness, Young's modulus and indentation fracture toughness. *iScience* **24**, 102735 (2021).

23. Masai, H. High-modulus oxide glasses fabricated by the melt-quenching method. *J. Ceram. Soc. Jpn*. **134**, 347–354 (2026).

24. Greer, A. L. Confusion by design. *Nature*, **366**, 303–304 (1993).

25. Yeh, J.-W. *et al.* Nanostructured high-entropy alloys with multiple principal elements: novel alloy design concepts and outcomes. *Adv. Eng. Mater.* **6**, 299–303 (2004).

26. Zhang, Y. *et al.* Microstructures and properties of high-entropy alloys. *Prog. Mater. Sci.* **61**, 1–93 (2014).

27. Hirata, A. *et al*. Geometric frustration of icosahedron in metallic glasses. *Science*, **341**, 376–379 (2011).

28. Nelcon, D. R. Order, frustration, and defects in liquids and glasses. *Phys. Rev. B* **28**, 5515–5535 (1983).

29. Ruessel, C. & Wisniewski, W. Glass-ceramic engineering: tailoring the microstructure and properties. *Prog. Mater. Sci.* **152**, 101437 (2025).

30. Masai, H. *et al.* Preparation of crystallized glass for application in fiber-type devices. *J. Mater. Res.* **24**, 288–293 (2009).

31. Price, D. L., Moss, S. C., Reijers, R., Saboungi, M.-L. & Susman, S. Intermediate-range order in glasses and liquids. *J. Phys. C: Solid State Phys.* **21**, L1069–L1072 (1988).

32. Salmon, P. S., Martin, R. A., Mason, P. E. & Cuello, G. J, Topological versus chemical ordering in network glasses at intermediate and extended length scales. *Nature* **435**, 75–78 (2005).

33. Yu, J. *et al*. Comprehensive structural study of glassy and metastable crystalline $BaTi_2O_5$. *Chem. Mater.* **21**, 259–263 (2009).

34. Arai, Y., Itoh, K., Kohara, S., & Yu, J. Refractive index calculation using the structural properties of $La_4Ti_9O_{24}$ glass. *J. Appl. Phys*. **103**, 094905 (2008).

35. Koyama, C. *et al.* Very sharp diffraction peak in nonglass-forming liquid with the formation of distorted tetraclusters. *NPG Asia Mater.* **12**, 43 (2020).

36. Shuseki, Y. *et al.* Atomic and electronic structure in MgO–SiO_2, *J. Phys. Chem. A*, **128**, 716–726 (2024).

37. Zeidler, A. *et al.*, Density-driven structural transformations in B_2O_3 glass. *Phys. Rev. B*, **90**, 024206 (2014).

38. Hashimoto, H. *et al.*, Structure of alumina glass, *Sci. Rep.*, **12**, 516 (2022).

39. Hashimoto, H. *et al.*, Bulk amorphous alumina: the density driven interplay of pentahedral pyramids and octahedra for high dielectric permittivity, *J. Am. Chem. Soc.*, **148**, 15826–15837 (2026).

40. Masai, H. *et al.* Photocatalytic hydrogen generation of monolithic porous titanium oxide-based glass–ceramics. *Sci. Rep.* **10**, 11615 (2020).

41. Wu, J. & Stebbins, J. F. Cation field strength effects on boron coordination in binary borate glasses. *J. Am. Ceram. Soc.* **97**, 2794–2801 (2014).

42. Deters, H. *et al.* Structural characterization of rare-earth-doped yttrium aluminoborate laser glasses using solid-state NMR. *J. Phys. Chem. C* **113**, 16216–16225 (2009).

43. Hayashi, K. *et al.* Melt-quenched oxide glasses with ultrahigh Young's modulus and small thermal expansion coefficient. *J. Am. Ceram. Soc.* **106**, 1732–1738 (2023).

44. Kohara S. & Suzuya K. Intermediate-range order in vitreous SiO_2 and GeO_2. *J. Phys. Condensed Matter.* **17**, S77-S86 (2005).

45. Bansal, N. P. & Doremus, R. H. Handbook of Glass Properties. (Academic Press, 1986).

46. Masai, H. Substitution effect of metal oxide on the elastic modulus of aluminoborate glasses. *J. Ceram. Soc. Jpn.* **134**, 576–585 (2026).

47. Shearer, A. *et al.* Zirconia-containing glass-ceramics: from nucleating agent to primary crystalline phase. *Int. J. Ceram. Eng. Sci.* **6**, e10200 (2024).

48. T. Rouxel, M. Huger, and J. L. Besson, Rheological Properties of YSiAlON Glasses- Elastic Moduli, Viscosity and Creep, *J. Mater. Sci.* **27**, 279–284 (1992).

49. J. Johnson, R. Weber, M. Grimsditch, Thermal and mechanical properties of rare earth aluminate and low-silica aluminosilicate optical glasses. *J. Non-Cryst. Solids*, **351**, 650 (2005).

50. Ritchie, R. O. The conflicts between strength and toughness. *Nat. Mater.* **10**, 817–822 (2011).

51. Masai, H., Fujii, Y., Kitamura, N. & Yamawaki, M. Relationship between the elastic properties and structure of $BaO–TiO_2–GeO_2–SiO_2$ glasses. *J. Non-Cryst. Solids* **576**, 121248 (2022).

52. Kohara, S. *et al.* Structural studies of disordered materials using high-energy x-ray diffraction from ambient to extreme conditions. *J. Phys.: Condens. Matter*. **19**, 506101 (2007).

53. Otomo, T. *et al.* Fundamental research of hydrogen storage mechanism with high-intensity total diffractometer. *KENS Rep*. **17**, 27 (2011).

54. Ravel, B. & Newville, M. ATHENA, ARTEMIS, HEPHAESTUS: data analysis for X-ray absorption spectroscopy using IFEFFIT. *J. Synchrotron Radiat*. **12**, 537−541 (2005).

55. Czjzek, G. *et al.* Atomic coordination and the distribution of electric field gradients in amorphous solids. *Phys. Rev. B.* **23**, 2513 (1981).

56. Srivastava, D. J., Giammar, M., Venetos, M. C., McCarthy-Carney, L., & Grandinetti, P. J. MRSimulator: A cross-platform, object-oriented software package for rapid solid-state NMR spectral simulation and analysis. *J. Chem. Phys.* **161**, 212501 (2024).

End Notes

Acknowledgements

This research was partially supported by the Japan Society for the Promotion of Science Grant-in-Aid for Scientific Research (B) (Number 22H01785) and for Transformative Research Areas (A) "Hyper-Ordered Structures Science" (Grant numbers 20H05878, 20H05881, 20H05882, and 23H04096) The author (H.M.) gratefully acknowledges the contributions of two technical staff members (Dr. N. Kitamura and Mr. H. Tomiki) who performed the experiments. The synchrotron radiation experiments were conducted at BL04B2 and BL14B2 of SPring-8 with the approval of the Japan Synchrotron Radiation Research Institute (JASRI) (Proposal numbers 2024B1004, 2024B1507, 2022B1971, and 2024B1976). The neutron experiments at the Materials and Life Science Facility of J-PARC were performed under a long-term proposal (Proposal number 2022L0202).

Author contributions

Design: HM; Methodology: HM, SK, YO; Investigation: HM, SK, YO, KK, TO; Sample preparation: HM; Writing—original draft, review & editing: HM, SK, YO, KK, TO. All authors have read and approved the final version of the manuscript.

Competing interests: The authors declare that they have no competing interests.

Data and materials availability: All relevant data supporting the findings of this study are available from the corresponding author upon request.

Supplementary Materials

Supplementary material for this article is available at XXXXXX.

Figure legends

Fig. 1 | Material characterization of MgO–Y_2O_3–(Ti, Zr)O_2–Al_2O_3–B_2O_3 glasses.

a, Differential thermal analysis (DTA) curves of powdered ID1–ID5 glass samples. Sample IDs are listed in Table 1. **b,** Crystallization onset temperature T_x (closed circles, left axis) and T_x- glass transition temperature T_g (open squares, right axis) as a function of the T_g, determined by powder DTA measurements. **c,** Optical absorption spectra of ID1–ID5 glasses in the visible region; the inset shows the corresponding spectra in the infrared region. **d,** Bright-field STEM image of the 5MgO–10Y_2O_3–10TiO_2–10ZrO_2–35Al_2O_3–30B_2O_3 (ID1) glass. **e,** High-angle annular dark-field (HAADF) STEM image of the same area as shown in panel d**. f,** Electron diffraction pattern of the ID1 glass.

Fig. 2 | Structural analysis of high-elastic oxide glass.

a, X-ray and neutron structure factor $S^{X,N}(Q)$ of 5MgO–10Y_2O_3–10TiO_2–10ZrO_2–35Al_2O_3–30B_2O_3 glass (ID1). **b,** Reduced pair distribution functions, $G^{X,N}(r)$ of the ID glass. Dotted line shows $G(r) = -4\pi r\rho_N$, where ρ_N is the number density. **c,** Total correlation functions $T^{X,N}(r)$ of the ID1 glass. Vertical dashed lines indicate peak positions observed in the neutron diffraction data. **d,** Zr K-edge XANES spectrum of the ID1 glass along with that of ZrO_2. Inset shows Fourier transform of EXAFS spectra of the ID1 glass along with ZrO_2 using the k range from 2.7 $Å^{-1}$ to 15.2 $Å^{-1}$. **e,** Y K-edge XANES spectrum of the ID1 glass along with that of Y_2O_3. Inset shows Fourier transform of EXAFS spectra of the ID1 glass along with Y_2O_3 using the k range from 2.5 $Å^{-1}$ to 12.5 $Å^{-1}$. **f,** Ti K-edge XANES spectrum of the ID1 glass along with that of anatase and rutile TiO_2. Inset shows Fourier transform of EXAFS spectra of the ID1 glass along with references using the k range from 1.8 $Å^{-1}$ to 10.0 $Å^{-1}$. **g,** ^{11}B MAS NMR spectra of the ID1 glass. **h,** ^{27}Al MAS NMR spectra of the ID1 glass. Dotted lines of both NMR spectra indicate each structural unit after peak deconvolution. **i**, Cation population of each structural unit in the ID1 glass. (NWF: network-forming unit).

Fig. 3 | Structure and crystallization behavior of glass-ceramics (G.Cs).

a, Comparison of the X-ray diffraction (XRD) patterns of the pristine 5MgO–10Y_2O_3–10TiO_2–10ZrO_2–35Al_2O_3–30B_2O_3 (ID1) glass with that of the ID1 glass-ceramic obtained by heat treatment at different

temperatures for 3 h. Inset shows a photographs of $5MgO–10Y_2O_3–10TiO_2–10ZrO_2–35Al_2O_3–30B_2O_3$ (ID1) glass-ceramics heat-treated at 790, 800, and 900 °C for 3 h. **b,** XRD patterns of the glass-ceramics (ID1–ID5) heat-treated at 850 °C for 3 h, together with reference patterns. **c,** 4D-STEM image of $4.5MgO–20Y_2O_3–5TiO_2–10.5ZrO_2–34Al_2O_3–24B_2O_3–1Li_2O–1SiO_2$ (ID4) glass-ceramic heat-treated at 850 °C for 3 h. Yellow and cyan squares indicate bright and dark area, respectively. **d,** Schematic illustration of multicomponent glass exhibiting atomistic heterogeneity. The orange and purple dotted ellipses highlight putative Ti- and Y-enriched nucleus-like regions, respectively, present prior to crystallization.

Fig. 4 | Elastic properties of high-elastic oxide glasses and glass-ceramics.

a, Young's modulus and Vickers hardness of the pristine glasses (thin bars) and the glass-ceramics obtained by heat-treatment at 850 °C for 3 h in air (bold bars). **b,** Comparison of Poisson's ratio between the pristine glasses (thin bars) and the corresponding glass-ceramics (bold bars). The numerical data plotted in Fig. 4a, b are provided in Supplementary Table 3. **c,** Relationship between Young's modulus and the T_g for the present glass samples, together with previously reported data[1, 18, 22, 23, 43, 48, 49] for comparison. Closed and open symbols denote melt-quenched and levitation-prepared glasses, respectively. The inset displays a photograph of the 0.58-mm-thick $1Li_2O–4.5MgO–20Y_2O_3–5TiO_2–10.5ZrO_2–34Al_2O_3–24B_2O_3–1SiO_2$ (ID4) glass-ceramic heat-treated at 850 °C for 3 h, with a Young's modulus of 195 GPa, under white-light illumination.

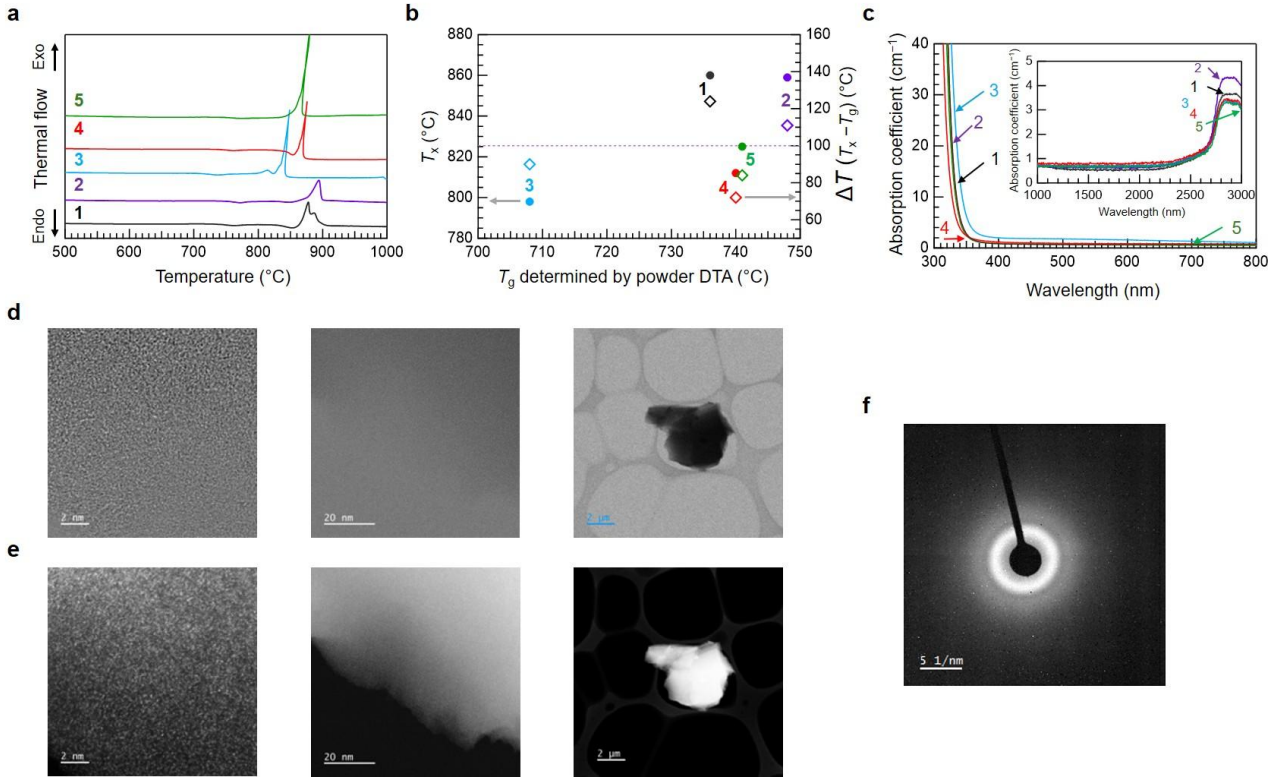


Fig. 1 | Material characterization of MgO–Y_2O_3–(Ti, Zr)O_2–Al_2O_3–B_2O_3 glasses.

a, Differential thermal analysis (DTA) curves of powdered ID1–ID5 glass samples. Sample IDs are listed in Table 1. **b,** Crystallization onset temperature T_x (closed circles, left axis) and T_x− glass transition temperature T_g (open squares, right axis) as a function of the T_g, determined by powder DTA measurements. **c,** Optical absorption spectra of ID1–ID5 glasses in the visible region; the inset shows the corresponding spectra in the infrared region. **d,** Bright-field STEM image of the 5MgO–10Y_2O_3–10TiO_2–10ZrO_2–35Al_2O_3–30B_2O_3 (ID1) glass. **e,** High-angle annular dark-field (HAADF) STEM image of the same area as shown in panel d**. f,** Electron diffraction pattern of the ID1 glass.

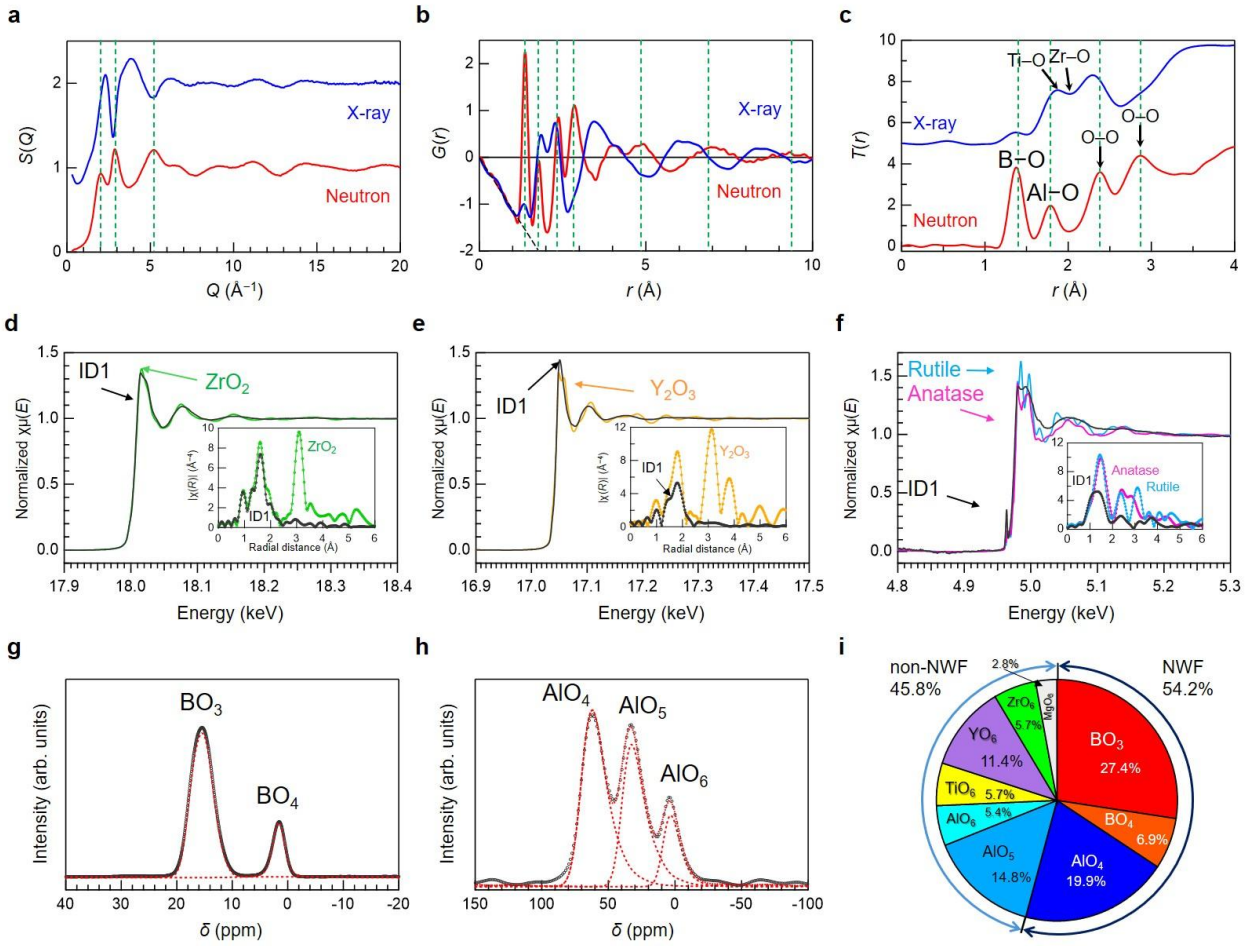


Fig. 2 | Structural analysis of high-elastic oxide glass.

a, X-ray and neutron structure factor $S^{X,N}(Q)$ of $5MgO–10Y_2O_3–10TiO_2–10ZrO_2–35Al_2O_3–30B_2O_3$ glass (ID1). **b,** Reduced pair distribution functions, $G^{X,N}(r)$ of the ID glass. Dotted line shows $G(r) = -4\pi r\rho_N$, where ρ_N is the number density. **c,** Total correlation functions $T^{X,N}(r)$ of the ID1 glass. Vertical dashed lines indicate peak positions observed in the neutron diffraction data. **d,** Zr K-edge XANES spectrum of the ID1 glass along with that of ZrO_2. Inset shows Fourier transform of EXAFS spectra of the ID1 glass along with ZrO_2 using the k range from 2.7 $Å^{-1}$ to 15.2 $Å^{-1}$. **e,** Y K-edge XANES spectrum of the ID1 glass along with that of Y_2O_3. Inset shows Fourier transform of EXAFS spectra of the ID1 glass along with Y_2O_3 using the k range from 2.5 $Å^{-1}$ to 12.5 $Å^{-1}$. **f,** Ti K-edge XANES spectrum of the ID1 glass along with that of anatase and rutile TiO_2. Inset shows Fourier transform of EXAFS spectra of the ID1 glass along with references using the k range from 1.8 $Å^{-1}$ to 10.0 $Å^{-1}$. **g,** ^{11}B MAS NMR spectra of the ID1 glass. **h,** ^{27}Al MAS NMR spectra of the ID1 glass. Dotted lines of both NMR spectra indicate each structural unit after peak deconvolution. **i**, Cation population of each structural unit in the ID1 glass. (NWF: network-forming unit).

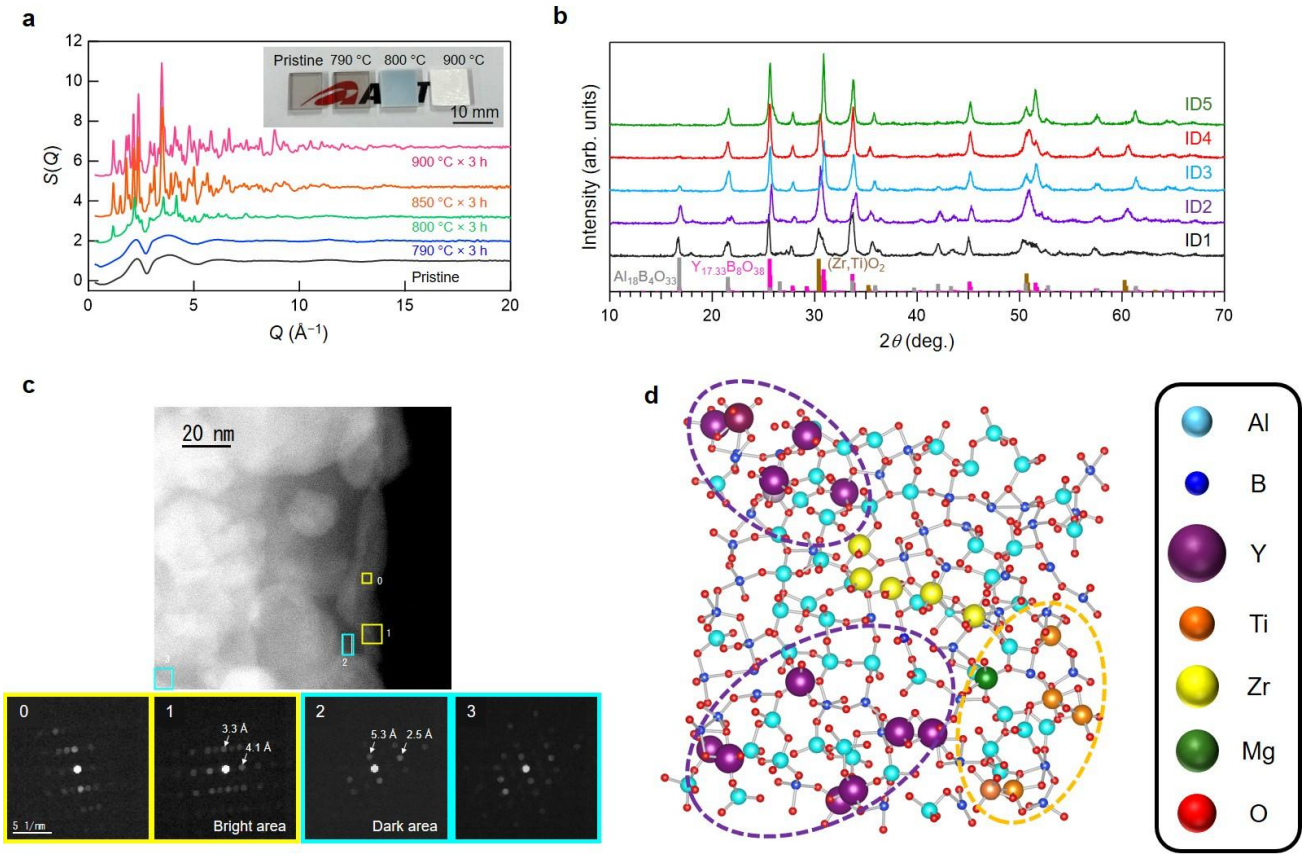


Fig. 3 | Structure and crystallization behavior of glass-ceramics (G.Cs).

a, Comparison of the X-ray diffraction (XRD) patterns of the pristine $5MgO–10Y_2O_3–10TiO_2–10ZrO_2–35Al_2O_3–30B_2O_3$ (ID1) glass with that of the ID1 glass-ceramic obtained by heat treatment at different temperatures for 3 h. Inset shows a photographs of $5MgO–10Y_2O_3–10TiO_2–10ZrO_2–35Al_2O_3–30B_2O_3$ (ID1) glass-ceramics heat-treated at 790, 800, and 900 °C for 3 h. **b,** XRD patterns of the glass-ceramics (ID1–ID5) heat-treated at 850 °C for 3 h, together with reference patterns. **c,** 4D-STEM image of $4.5MgO–20Y_2O_3–5TiO_2–10.5ZrO_2–34Al_2O_3–24B_2O_3–1Li_2O–1SiO_2$ (ID4) glass-ceramic heat-treated at 850 °C for 3 h. Yellow and cyan squares indicate bright and dark area, respectively. **d,** Schematic illustration of multicomponent glass exhibiting atomistic heterogeneity. The orange and purple dotted ellipses highlight putative Ti- and Y-enriched nucleus-like regions, respectively, present prior to crystallization.

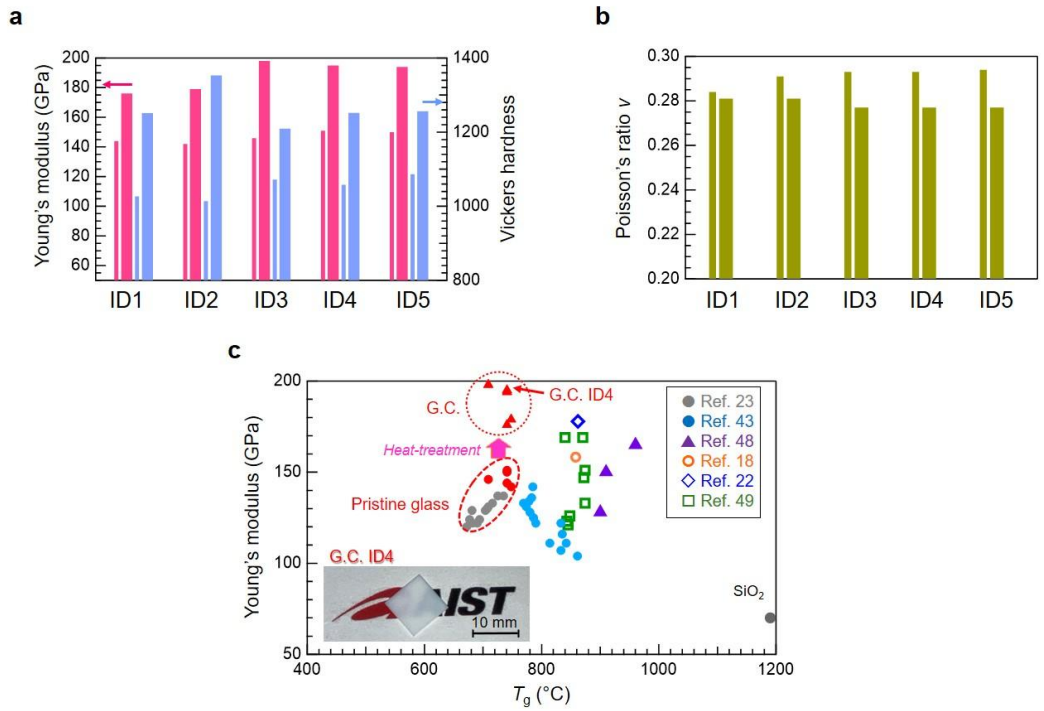


Fig. 4 | Elastic properties of high-elastic oxide glasses and glass-ceramics.

a, Young's modulus and Vickers hardness of the pristine glasses (thin bars) and the glass-ceramics obtained by heat-treatment at 850 °C for 3 h in air (bold bars). **b,** Comparison of Poisson's ratio between the pristine glasses (thin bars) and the corresponding glass-ceramics (bold bars). The numerical data plotted in Fig. 4a, b are provided in Supplementary Table 3. **c,** Relationship between Young's modulus and the T_g for the present glass samples, together with previously reported data[1, 18, 22, 23, 43, 48, 49] for comparison. Closed and open symbols denote melt-quenched and levitation-prepared glasses, respectively. The inset displays a photograph of the 0.58-mm-thick $1Li_2O–4.5MgO–20Y_2O_3–5TiO_2–10.5ZrO_2–34Al_2O_3–24B_2O_3–1SiO_2$ (ID4) glass-ceramic heat-treated at 850 °C for 3 h, with a Young's modulus of 195 GPa, under white-light illumination.

Table 1. Chemical compositions and physical properties of the $MgO–Y_2O_3–(Ti, Zr)O_2–Al_2O_3–B_2O_3$ glasses (glass transition temperature, T_g; coefficient of thermal expansion, CTE).

Sample ID		1	2	3	4	5
Composition (mol%)	MgO	5	5	4.5	4.5	4
	Y_2O_3	10	10	19	20	20
	TiO_2	10	5	9	5	9
	ZrO_2	10	15	9	10.5	9
	Al_2O_3	35	35	30	34	32.5
	B_2O_3	30	30	25	24	23
	SiO_2	0	0	2.5	1	1.5
	Li_2O	0	0	1	1	1
Density ($g \cdot cm^{-3}$)		3.46	3.53	3.77	3.83	3.84
Glass transition temperature T_g (°C)		741	748	709	740	741
Coefficient of thermal expansion ($\times 10^{-6} K^{-1}$)		6.7	6.8	7.5	7.2	7.5
Longitudinal sound velocity V_L ($km \cdot s^{-1}$)		7.33	7.28	7.15	7.22	7.19
Transverse sound velocity V_T ($km \cdot s^{-1}$)		4.02	3.95	3.87	3.90	3.88
Shear Modulus G_0 (GPa)		56.1	55.1	56.5	58.5	57.9
Poisson's Ratio v		0.284	0.291	0.293	0.293	0.294
Young Modulus E_0 (GPa)		144	142	146	151	150
Bulk Modulus K_0 (GPa)		111	113	118	122	121
Hv0.2		1027	1014	1072	1058	1086

Supplementary Files

This is a list of supplementary files associated with this preprint. Click to download.

- Supplementarydataset.docx